Versatility of doped nanocrystalline silicon oxide for applications in silicon thin-film and heterojunction solar cells

Alexei Richter[I], Vladimir Smirnov[I], Andreas Lambertz[I], Keita Nomoto[II], Katharina Welter[I], and Kaining Ding[I]

[I]Institute of Energy and Climate Research 5-Photovoltaik, Forschungszentrum Jülich GmbH, 52425 Jülich, Germany

[II]School of Aerospace, Mechanical and Mechatronic Engineering, Faculty of Engineering and Information Technologies, The University of Sydney, Sydney, Australia

Corresponding author:
Alexei Richter
phone: +49 2461 61-5600, fax: +49 2461 61-3735, email: ale.richter@fz-juelich.de

Keywords

Nanocrystalline silicon oxide; silicon heterojunction solar cells; multi-junction thin-film solar cells; atom probe tomography ; photon management

Abstract

To optimize the optical response of a solar cell, specifically designed materials with appropriate optoelectronic properties are needed. Owing to the unique microstructure of doped nanocrystalline silicon oxide, nc-SiO_x:H, this material is able to cover an extensive range of optical and electrical properties. However, applying nc-SiO_x:H thin-films in photovoltaic devices necessitates an individual adaptation of the material properties according to the specific functions in the device. In this study, we investigated the detailed microstructure of doped nc-SiO_x:H films via atom probe tomography at the sub-nm scale, thereby, for the first time, revealing the three-dimensional distribution of the nc-Si network. Furthermore, n- and p-type nc-SiO_x:H layers with various optical and electrical properties were implemented as a window, back contact, and an intermediate reflector layer in silicon heterojunction and multi-junction thin-film solar cells with a focus on the key aspects for adapting the material properties to the specific functions. Here, nc-SiO_x:H effectively reduced the parasitic absorption and opened new possibilities for the photon management in the solar cells, thereby, demonstrating the versatility of this material. Remarkably, using our adapted nc-SiO_x:H layers in distinct functions enabled us to achieve a combined short circuit current density of 15.1 mA cm^{-2} for the two a-Si:H sub-cells in an a-Si:H/a-Si:H/μc-Si:H triple-junction thin-film solar cell and an active area efficiency of 21.4 % was realized for a silicon heterojunction solar cell.

1. Introduction

Hydrogenated nanocrystalline silicon oxide (nc-SiO_x:H), often also called microcrystalline silicon oxide (μc-SiO_x:H), attracts significant attention as a material for photovoltaics [1–6]. The unabated interest in doped, both n- and p-type, nc-SiO_x:H prevails mainly due to its remarkable variability. Particularly, the optical and electrical properties of this material can be varied in a broad range, providing a tunable refractive index, a low absorption coefficient in the relevant energy range, and a sufficient electrical conductivity. This is made possible by its characteristic microstructure, which is usually described as comprising of well conducting filaments or pearl-chain like arrangements of nanocrystalline silicon (nc-Si) embedded in a highly transparent, oxygen rich amorphous silicon oxide (a-SiO_x:H) matrix as indicated by TEM investigations [1,2,7,8]. As a result, nc-SiO_x:H is widely applicable as a window, back contact (BC) or intermediate reflector (IR) layer in various solar cell concepts. So far, nc-SiO_x:H has been utilized in photovoltaic devices like thin-film (TF) silicon solar cells [3,9–11], multi-junction solar cells [12–14], crystalline silicon solar cells with diffused emitters [6], and silicon heterojunction (SHJ) solar cells [15–18]. Each of these applications requires specific optoelectronic properties in order to improve the overall spectral utilization and the response of the solar cell. In this study, we investigate the microstructure of device relevant nc-SiO_x:H n- and p-type nc-SiO_x:H films by atom probe tomography (APT) revealing the three-dimensional network structure of nc-Si in nc-SiO_x:H for the first time. Furthermore, we present our most recent results on SHJ and triple-junction TF solar cells employing n- and p-type nc-SiO_x:H films.

2. Materials and methods

The n- and p-type nc-SiO_x:H TFs described in this study were deposited on Corning Eagle 2000 glass substrates via plasma enhanced chemical vapor deposition (PECVD) at a plasma frequency of 13.56 MHz (RF). While the substrate temperature was around 185 °C and the power density was fixed at around 300 mW cm^{-2}. The deposition pressure was set to 4 mbar. Silane (SiH_4), hydrogen (H_2), methane (CH_4), and carbon dioxide (CO_2) served as precursor gases and the n- and p-type doping of the films were achieved by adding phosphine PH_3 or trimethylborane $B(CH_3)_3$, respectively. The composition of the gas mixture during the deposition was characterized by the silane concentration *SC* and the CO_2 gas flow ratio r_{CO2}, defined by $SC = \frac{[SiH_4]}{[H_2]+[SiH_4]}$ and $r_{CO_2} = \frac{[CO_2]}{[CO_2]+[SiH_4]}$, respectively.

To evaluate the properties of the nc-SiO_x:H films, the thickness was measured using a Vecco DEKTAK 6M Stylus Profiler. Here, the thickness of the deposited films ranged from 0.3 to about 1 μm. The electrical performance was evaluated by determining the lateral dark conductivity σ_D with coplanar silver contacts. To describe the optical properties of the films, the spectral transmittance and reflectance were obtained using a Perkin Elmer LAMBDA 950 spectrometer. Afterwards, the spectral absorption coefficient $\alpha(\lambda)$ was evaluated [19] to determine the optical band gap E_{04} at $\alpha = 10^4$ cm^{-1}. Furthermore, the refractive index $n(\lambda)$ was determined using the Fresnel equation. Additionally, photo thermal deflection spectroscopy (PDS) was employed to determine the E_{04} and *n* of highly transparent films.

Specimen for the Atom Probe Tomography (APT) investigations were prepared by using a Zeiss Auriga focused ion beam electron microscope (FIB-SEM). Before, a 300 nm layer of Pt was deposited on the films to prevent damage from Ga ions during the FIB milling. More details on the sample preparation can be found in [20]. The measurements were performed on a CAMECA LEAP 4000Xsi with a pulsed 355 nm laser (250 kHz, 50 pJ) and an overall detection efficiency of 57 %. During the APT measurements the sample holder was cooled to

40 K at a chamber pressure below 10^{-9} Pa. In the last step, CAMECA's IVAS software was used for reconstruction and analysis of the sample data.

All wafers used for the SHJ solar cells were cleaned by sulfuric acid and hydrogen peroxide (96 and 30 %, respectively) in a ratio of 2:1 for 10 min followed by a 2 min dip in 1 % hydrofluoric acid (HF) prior to deposition. The cells were deposited on (100)-oriented wet chemically textured CZ silicon wafers (170 µm, 1-5 Ω cm). After cleaning, 5 nm of intrinsic a-Si:H layers were deposited via PECVD to passivate the wafer surface at a substrate temperature of 140 °C and a deposition pressure of 1 mbar, using SiH_4 and H_2 as process gases, the power density was set to 18 mW cm^{-2} with an electrode distance of 23 mm at 13.56 MHz. The deposition was followed by a thermal annealing step in ambient air at 220°C. After a short HF dip, the n- and p-type nc-SiO_x:H layers were deposited at the conditions outlined above. Then, the area of each cell on the wafer was defined by sputtering indium tin oxide (ITO) through a shadow mask on each side at a substrate temperature of 125 °C. An ITO target with 5 wt. % SnO_2 was used at a deposition pressure of 50 mPa. Following the ITO deposition, silver grids were evaporated onto the cells through shadow masks. On the back side a full area silver contact was evaporated for each cell. Lastly, the cells were thermally annealed in air for 2 h at 220 °C. The full layer stack of the SHJ solar cells has been described in [21].

For the TF silicon solar cells SnO_2:F coated glass from the Asahi Glass company was used as a substrate to deposit cells in a p-i-n configuration. The schematic layer stack is depicted in Fig. 1 b). The exact deposition parameters for the a-SiC:H, a-Si:H and µc-Si:H layers can be found in [9,10,13,22].

To characterize the solar cells, a double source AM1.5 solar simulator (Class A) was used at standard test conditions (AM1.5G, 1 kW m^{-2}, 25 °C). Furthermore, external quantum efficiency *EQE* spectra were measured using a differential spectral response (DSR) setup. More details on the measurement of the multi-junction solar cells can be found in [13]. Additionally, by convoluting the *EQE* spectra with the AM1.5G solar spectrum in the range from 350 to 1150 nm, the active area short circuit current density J_{sc} was calculated. The reflectance *R* was measured using the Perkin Elmer LAMBDA 950 spectrometer.

3. Results

Various possible applications of nc-SiO_x:H layers in silicon heterojunction (SHJ) and Si thin-film (TF) solar cells are sketched in Fig. 1 a) and b), respectively. At the illuminated side of a SHJ solar cell layers of nc-SiO_x:H can be used as front-emitter or front surface field (FSF) layers ("I" in Fig. 1 a)). The main focus in this application is to reduce the parasitic absorption at the front of the solar cell due to the high transparency of nc-SiO_x:H layers in comparison to a-Si:H [8,15,21]. At the same time, the conductivity of the employed layers has to be sufficient to maintain a high fill factor (*FF*) in the device. Furthermore, nc-SiO_x:H can be used at the rear of SHJ solar cells to serve as a rear-emitter layer [21] or a back surface field [23] ("II" in Fig. 1 a)). Here, a high conductivity and a low contact resistance towards the transparent conductive oxide (TCO) are paramount.

In multi-junction Si TF solar cells nc-SiO_x:H layers can be applied at the back of the top sub-cell ("III" in Fig. 1 b)) as a first interlayer, which mainly serves to reduce the parasitic absorption of light at this part of the solar cell. A well-balanced trade-off between a high transparency and a sufficient conductivity is required for these films similarly to the application as a FSF or a front-emitter layer. An intermediate reflector ("IV" in Fig. 1 b)) is

another possible application of nc-SiO_x:H layers in multi-junction Si TF solar cells. By using specifically optically tuned nc-SiO_x:H layers, these allow to match the generated current between the adjoining sub-cells in a multi-junction solar cell by introducing an abrupt change in *n* [24,25]. Furthermore, nc-SiO_x:H layers can reduce the parasitic absorption at the rear of Si TF solar cells when applied as back contact layers (BC, "V" in Fig. 1 b)) [10]. Here, the nc-SiO_x:H layer reduces the parasitic absorption by surface plasmons in the metal contact [26,27] and a well-balanced compromise between a low refractive index *n* and a high electrical conductivity has to be found.

In order to fulfill the mentioned requirements for each application, the properties of the nc-SiO_x:H layers have to be tuned. Fig. 2 summarizes the development of a wide variety of nc-SiO_x:H films. In detail, the dark electrical conductivity (σ_D) is presented versus the refractive index *n* in Fig. 2 a) and versus the optical band gap E_{04} in Fig. 2 b). The *n* values achievable in these layers ranged from 3.6 to 1.9. Similarly, E_{04} could be varied from about 1.9 eV to almost 2.9 eV. All the while, σ_D changed by many orders of magnitude from 10^{-12} $(\Omega\ cm)^{-1}$ close to 10^{2} $(\Omega\ cm)^{-1}$. Typically, an increase in E_{04}, accompanied by a lowered *n*, leads to a decrease in σ_D. Furthermore, Fig. 2 shows that improved optoelectronic properties could be achieved with n-type nc-SiO_x:H films as compared to p-type nc-SiO_x:H, resulting in a higher E_{04} at any given σ_D or vice versa. Three films of nc-SiO_x:H are highlighted in this plot as stars to indicate layers that were suitable to serve as a FSF layer, an emitter layer, a BC layer, or an IR in Si TF or SHJ solar cells. Please note that the σ_D of the thin nc-SiO_x:H films used in solar cells is expected to be lower than the value determined from thicker (several hundred nm) films [28]. Nevertheless, the properties determined on thicker films have proven to serve well as indicators for the suitability of a nc-SiO_x:H film in a desired application.

The key requirements for the different applications are summarized in Table 1 and are related to the properties of the highlighted films from Fig. 2. Accordingly, the nc-SiO_x:H film "A" with well-balanced optoelectronic properties ($E_{04} \approx 2.25$ eV, $\sigma_D \approx 10^{-2}$ $(\Omega\ cm)^{-1}$) was most suitable for the application as a FSF and as a BC layer. In contrast, film "B" ($\sigma_D \approx 10^{-1}$ $(\Omega\ cm)^{-1}$) offered the electrical conductivity demanded by the application as a rear-emitter layer or a back surface field (BSF). Lastly, the required low *n* for an IR layer was achieved by film "C" with $n \approx 2$.

The microstructure of an n-type and a p-type nc-SiO_x:H film with similar properties and composition as the films "A" and "B" from Fig. 2, respectively, were investigated via APT. APT is a destructive, sub-nm imaging technique that is based on the effects of field evaporation and field ionization of atoms from an nm sized needle of the investigated material. Due to intrinsic design limitations of the microchannel plates and effects like de - ionization of ions only a limited fraction of the evaporated atoms can be collected, resulting in detection efficiencies around 60 % [29,30]. Even though the investigated films were deposited at slightly different deposition conditions [21], their microstructure can be taken as a suitable

Table 1: Requirements on thin films for different applications and the compliance of selected nc-SiO_x:H layers, presented in Fig. 2, with those requirements. The symbols -, 0, and + indicate a low, moderate, and excellent compliance, respectively. The high transparency refers to the short wavelength range below 600 nm.

application				key requirement	nc-SiO_x:H		
FSF / emitter	BSF / emitter	IR	BC		A	B	C
!				high transparency	**0**	**-**	**+**
!	!		!	high conductivity	**0**	**+**	**-**
		!	!	low refractive index	**0**	**-**	**+**

representation for similar n- and p-type nc-SiO_x:H films. The obtained microstructures of the films are displayed in Fig. 3. Here, the nc-Si phase was approximated by defining a threshold density of 49.9 nm^{-3} of Si for a given voxel size of 0.5x0.5x0.5 nm^3, while considering the detector efficiency of the APT measurement. A similar distribution of the nc-Si phase has been previously observed by high resolution transmission electron microscopy (HRTEM) at a comparable scale [1,2,14], supporting the Si density approximation for the nc-Si phase used here. Accordingly, Si iso density surfaces were constructed by connecting voxels attributed to the nc-Si phase. The, thereby, defined areas of nc-Si show Si filaments, elongated in growth direction of the films for n-type as well as p-type nc-SiO_x:H films. The filaments were up to 5 nm thick and were separated by Si deficient areas, which mostly correlated with the positions of O-rich areas (not shown). Overall, a lower amount of nc-Si was evident in the p-type nc-SiO_x:H film as compared to the n-type film in Fig. 3. The crystalline volume fractions could be estimated by relating the number of atoms within the approximated nc-Si phase to the total number of detected atoms, yielding a crystalline volume fraction of 27 % for the n-type film and 20 % for the p-type material. The three-dimensional network of the Si iso density surfaces is presented in Fig. 4 a) and b). Both nc-SiO_x:H films contained an extensively interconnected network of nc-Si with a predominant orientation in the direction of film growth. Using a proximity histogram analysis the average positions of the dopant atoms were identified with respect to the nc-Si surfaces (Fig. 4 c) and d)). Similar concentrations of the dopant atoms were detected within the nc-Si phase as well as the surrounding matrix for both types of films. At the same time, significant amounts of C were found within the nc-SiO_x:H films. Especially the p-type nc-SiO_x:H film contained up to 1.5 at. % of C within the matrix phase.

In a next step the investigated nc-SiO_x:H films were applied in a SHJ and an a-Si:H/a-Si:H/µc-Si:H triple-junction TF solar cell to illustrate the potential of the nc-SiO_x:H layers in their various functions. Fig. 5 displays the external quantum efficiency (EQE) and the absorptance (A) of the rear-emitter SHJ solar cell with the n-type nc-SiO_x:H ("A" in Fig. 2) as a FSF layer and the p-type nc-SiO_x:H ("B" in Fig. 2) as a rear-emitter layer. An active area efficiency η_{act} of 21.4 % for the best cell was achieved on a Si random pyramid textured 170 µm CZ Si wafer with an active area of approximately 3.4 cm^2 without any further optical or electrical optimization of the individual layers or their thicknesses as compared to non-textured solar cells [21].

In an a-Si/a-Si/µc-Si triple-junction solar cell a remarkably high combined J_{sc} of 15.1 mA cm^{-2} could be achieved for the two front sub-cells, using a-Si:H absorber layers, by employing an nc-SiO_x:H layer with a low n of 2 and $\sigma_D \approx 10^{-4}$ $(\Omega\ cm)^{-1}$ ("C" in Fig. 2) as an IR between the middle and the bottom sub-cell. The corresponding *EQE* and the solar cell parameters are shown in Fig. 6. Additionally, this solar cell used an n-type nc-SiO_x:H layer ("A" in Fig. 2) as a BC layer to reduce the parasitic absorption at the rear.

4. Discussion

The advantageous tunability of nc-SiO_x:H films gives rise to a wide range of possible applications. Depending on the requirements of the specific function, the optoelectronic properties, characterized by E_{04}, n, and σ_D, have to be adjusted [22]. We achieved this by changing the *SC* and r_{CO2}. These affect the fractions of crystalline Si and a-SiO_x:H within the film and thereby the properties of the nc-SiO_x:H [1,11,14,31,32]. Generally, an increase in r_{CO2} yields more transparent, but also less conductive films, due to an increased oxygen content [1,31], while a higher *SC* leads to an increase in σ_D due to an increasing volume fraction of nc-Si for a sufficiently low r_{CO2} [14,31,33].

The APT investigation revealed an anisotropic nc-Si network in growth direction of the film for n-type as well as p-type nc-SiO_x:H. It is important to note that different evaporation fields and surface curvatures for the different phases could have produced so called “local magnification effects” and trajectory aberrations [29,34]. These effects might distort the origin of a given ion and affect the reliability of the calculated atom densities and therefore the phase identification. However, a similar anisotropic microstructure has been observed by HRTEM [1,2,14] which qualitatively confirms the determined distribution of the nc -Si phase. Now, a detailed three-dimensional distribution of the nc-Si network could be reconstructed via APT, thereby revealing a large amount of lateral connections within the nc-Si network that explain the high lateral σ_D of both films. At the same time, a higher conductivity can be expected in the transversal direction due to the preferential orientation of the nc-Si in this direction, which is crucial for the performance in a solar cell. The distribution of nc-Si was similar for both films, although the volume fraction of nc-Si was less in the p-type material. The lower crystallinity of the p-type material is probably related to the amorphization effect by the B [8,13,35,36].

The detailed dopant distribution within the nc-SiO_x:H films could be explored by APT as well. Both, P and B, were found to be distributed nearly equally across both phases. This is in contrast to thermally grown films of Si nanocrystalls embedded in a SiO_2 matrix where an increased P content was found in the Si nanocrystalls for n-type material and a decreasing amount of B towards the inner part of the nanocrystalline Si for p-type material [20]. A possible cause might be a lack of time and/or energy provided to the system during PECVD to rearrange the dopant atoms to their thermodynamically favorite sites. Furthermore, the uncertainties in determining the nc -Si phase (and thereby its surface) by APT, as mentioned previously, affect the accuracy of the proximity histograms. Despite similar dopant concentrations, the dopants in the amorphous matrix phase are expected to be mostly inactive due to an insufficient coordination. Furthermore, the charge carrier mobility within the matrix phase can be assumed to be significantly lower than in the nc-Si phase due to a higher degree of disorder in the amorphous matrix. Therefore, the high σ_D is attributed to the nc-Si network. The main incorporation of C presumably from the doping gas trimethylboron, especially in the O-rich matrix, could be detected for the p-type nc -SiO_x:H film which has also been reported at about 2 at. % by other authors [7,31]. This C could contribute to a reduced amount of nc-Si phase in favor of the amorphous phases within the films [37] in addition to the amorphization by B. Thereby, slightly increasing E_{04} and reducing σ_D of the films. The incorporation of C in the n-type nc -SiO_x:H film probably stems from using CO_2 as the O source. Although most of the C is expected to leave the deposition chamber in the form of CO or CO_2 [38], a small amount is still embedded in the film.

In the solar cell the strong anisotropic growth of the nc-Si phase leads to a good transversal conductivity, so that the O-rich a-SiO_x:H phase can provide a high transparency while the electrical current is mainly carried by the doped nc-Si network. This is beneficial independently of the specific application. However, the amount of the individual phases can be tuned to achieve the desired properties. At the front of a SHJ and a Si TF solar cell the n-type nc-SiO_x:H films reduce the parasitic absorption as a FSF, a front-emitter layer, or interlayers in general due to their high E_{04}, while as a back contact layer on the rear of a Si TF solar cell they reduce the parasitic absorption related to plasmonic losses in the reflector [26,27]. Applied in a textured rear-emitter SHJ solar cell a high J_{sc} of 39.4 mA cm^{-2} is demonstrating the benefit of implementing the transparent nc-SiO_x:H FSF layer. At the same time, a *FF* of about 75 % demonstrates that the p-type nc-SiO_x:H film provides a good contact towards the rear-ITO as a rear-emitter layer in the SHJ solar cell thanks to the extensive network of nc-Si and a corresponding σ_D. In comparison to our previous results obtained on planar substrates [21], we significantly increased the J_{sc} by exploiting the superior light

incoupling and light trapping of textured wafers and, at the same time, enhanced the V_{oc} by reducing the wafer thickness from 280 to 170 µm [39].

As an IR in a multi-junction solar cell the n-type nc-SiO_x:H film "C" from Fig. 2 offered a high contrast in *n* with respect to the n-type a-Si:H layer above it, thereby effectively increasing the reflection of light towards the sub-cells above the IR. Accordingly, a high combined current of 15.1 mA cm^{-2} was achieved for the first and the second a-Si:H sub-cell, which is comparable to a-Si/a-Si tandem solar cells with silver back reflectors [40]. Furthermore, an *FF* of 74 % was achieved in the triple junction solar cell. Here, the low σ_D of the nc-SiO_x:H IR is accompanied by an increased defect density, which is beneficial for its secondary function as a recombination junction. Additionally, using an optoelectronically balanced nc-SiO_x:H BC layer gave rise to a reduced parasitic absorption at the back of this solar cell.

5. Conclusion

Within this work we presented the numerous applications of nc-SiO_x:H films in silicon heterojunction (SHJ) and silicon thin-film (TF) solar cells, making use of their remarkable versatility. In particular, an intricate three-dimensional network of nc-Si is providing conductive paths for the electrical current in lateral as well as transversal direction, while an O-rich matrix phase provides a high E_{04} and a low *n*. Here, the dopant atoms are nearly randomly distributed across all phases in the n-type as well as the p-type material. A wide range of properties can be achieved by the nc-SiO_x:H layers by adjusting this microstructure. In detail, the application as a window, front-emitter or back contact (BC) layer demands a nc-SiO_x:H layer with well-balanced optoelectronic properties, while the rear-emitter layer in a SHJ solar cell has to be highly conductivity in order to ensure a good contact towards the TCO. In contrast, for a nc-SiO_x:H intermediate reflector (IR) a lower conductivity is tolerable to achieve a low refractive index. Combining the beneficial properties of nc-SiO_x:H as an IR and BC layer, an a-Si/a-Si/µc-Si triple-junction TF solar cell with a combined short circuit current of 15.1 mA cm^{-2} for the two a-Si:H sub-cells and a *FF* of 74 % was presented. Furthermore, an n-type nc-SiO_x:H FSF layer and a p-type nc-SiO_x:H rear-emitter layer led to a textured rear-emitter SHJ solar cell with an active area efficiency of 21.4 %.

6. Acknowledgements

The authors would like to thank M. Meyer for her contributions to producing the SHJ solar cells. We are also grateful to S. Moll, W. Reetz, C. Zahren, F. Lentz, M. Meier, H. Siekmann, S. Haas, A. Bauer, G. Schöpe, S. Kasper, J. Klomfaß, O. Thimm, A. Gerber, and B. Turan for their assistance in fabricating and characterizing the thin-film solar cells. Furthermore, K. Nomoto acknowledges the facilities and the scientific and technical assistance of the Australian Microscopy & Microanalysis Research Facility at the Australian Centre for Microscopy & Microanalysis at the University of Sydney.

7. List of references

[1] V. Smirnov, A. Lambertz, S. Moll, M. Bär, D.E. Starr, R.G. Wilks, M. Gorgoi, A. Heidt, M. Luysberg, B. Holländer, F. Finger, Doped microcrystalline silicon oxide alloys for silicon-based photovoltaics: Optoelectronic properties, chemical composition, and structure studied by advanced characterization techniques, Phys. Status Solidi. 213 (2016) 1814–1820.

[2] M. Klingsporn, S. Kirner, C. Villringer, D. Abou-Ras, I. Costina, M. Lehmann, B. Stannowski, Resolving the nanostructure of plasma-enhanced chemical vapor deposited nanocrystalline SiOx layers for application in solar cells, J. Appl. Phys. 119 (2016) 223104.

[3] C. Shin, S.M. Iftiquar, J. Park, S. Ahn, S. Kim, J. Jung, S. Bong, J. Yi, Radio frequency plasma deposited boron doped high conductivity p-type nano crystalline silicon oxide thin film for solar cell window layer, Mater. Chem. Phys. 159 (2015) 64–70.

[4] S. Kirner, O. Gabriel, B. Stannowski, B. Rech, R. Schlatmann, The growth of microcrystalline silicon oxide thin films studied by in situ plasma diagnostics, Appl. Phys. Lett. 102 (2013) 51906.

[5] M. Izzi, M. Tucci, L. Serenelli, P. Mangiapane, M. Della Noce, I. Usatii, E. Esposito, L.V. Mercaldo, P. Delli Veneri, Doped SiOx emitter layer in amorphous/crystalline silicon heterojunction solar cell, Appl. Phys. A Mater. Sci. Process. 115 (2014) 705–712.

[6] J. Stuckelberger, G. Nogay, P. Wyss, Q. Jeangros, C. Allebé, F. Debrot, X. Niquille, M. Ledinsky, A. Fejfar, M. Despeisse, F.-J. Haug, P. Löper, C. Ballif, Passivating electron contact based on highly crystalline nanostructured silicon oxide layers for silicon solar cells, Sol. Energy Mater. Sol. Cells. 158 (2016) 2–10.

[7] P. Cuony, D.T.L. Alexander, I. Perez-Wurfl, M. Despeisse, G. Bugnon, M. Boccard, T. Söderström, A. Hessler-Wyser, C. Hébert, C. Ballif, Silicon filaments in silicon oxide for next-generation photovoltaics, Adv. Mater. 24 (2012) 1182–1186.

[8] K. Ding, U. Aeberhard, V. Smirnov, B. Holländer, F. Finger, U. Rau, Wide Gap Microcrystalline Silicon Oxide Emitter for a-SiOx:H/c-Si Heterojunction Solar Cells, Jpn. J. Appl. Phys. 52 (2013) 122304.

[9] A. Lambertz, T. Grundler, F. Finger, Hydrogenated amorphous silicon oxide containing a microcrystalline silicon phase and usage as an intermediate reflector in thin-film silicon solar cells, J. Appl. Phys. 109 (2011) 113109-1-113109–10.

[10] A. Lambertz, F. Finger, R.E.I. Schropp, U. Rau, V. Smirnov, Preparation and measurement of highly efficient a-Si:H single junction solar cells and the advantages of μc-SiOx:H n-layers, Prog. Photovoltaics Res. Appl. 23 (2015) 939–948.

[11] A. Lambertz, F. Finger, B. Hollaender, J.K. Rath, R.E.I. Schropp, Boron-doped hydrogenated microcrystalline silicon oxide (μc-SiOx:H) for application in thin-film silicon solar cells, J. Non. Cryst. Solids. 358 (2012) 1962–1965.

[12] P. Delli Veneri, L.V. Mercaldo, I. Usatii, Improved micromorph solar cells by means of mixed-phase n-doped silicon oxide layers, Prog. Photovoltaics Res. Appl. 21 (2013) 148–155.

[13] V. Smirnov, A. Lambertz, S. Tillmanns, F. Finger, p- and n-type microcrystalline

silicon oxide (μc-SiOx:H) for applications in thin film silicon tandem solar cells, Can. J. Phys. 92 (2014) 932–935.

[14] H. Tan, P. Babal, M. Zeman, A.H.M. Smets, Wide bandgap p-type nanocrystalline silicon oxide as window layer for high performance thin-film silicon multi-junction solar cells, Sol. Energy Mater. Sol. Cells. 132 (2015) 597–605.

[15] L. Mazzarella, S. Kirner, B. Stannowski, L. Korte, B. Rech, R. Schlatmann, p-type microcrystalline silicon oxide emitter for silicon heterojunction solar cells allowing current densities above 40 mA/cm2, Appl. Phys. Lett. 106 (2015) 23902.

[16] K. Ding, U. Aeberhard, A. Lambertz, V. Smirnov, B. Holländer, F. Finger, U. Rau, Impact of doped microcrystalline silicon oxide layers on crystalline silicon surface passivation 1, Can. J. Phys. 92 (2014) 758–762.

[17] K. Nakada, S. Miyajima, M. Konagai, Application of n-type microcrystalline silicon oxide as back reflector of crystalline silicon heterojunction solar cells, Jpn. J. Appl. Phys. 54 (2015) 82301.

[18] S.Y. Herasimenka, W.J. Dauksher, M. Boccard, S. Bowden, ITO/SiOx:H stacks for silicon heterojunction solar cells, Sol. Energy Mater. Sol. Cells. 158 (2016) 98–101.

[19] Y. Hishikawa, N. Nakamura, S. Tsuda, S. Nakano, Y. Kishi, Y. Kuwano, Interference-free determination of the optical absorption coefficient and the optical gap of amorphous silicon thin films, Jpn. J. Appl. Phys. 30 (1991) 1008–1014.

[20] K. Nomoto, H. Sugimoto, A. Breen, A.V. Ceguerra, T. Kanno, S.P. Ringer, I.P. Wurfl, G.J. Conibeer, M. Fujii, Atom Probe Tomography Analysis of Boron and/or Phosphorus Distribution in Doped Silicon Nanocrystals, J. Phys. Chem. C. 120 (2016) 17845–17852.

[21] A. Richter, F. Lentz, M. Meier, F. Finger, K. Ding, Light management in planar silicon heterojunction solar cells via nanocrystalline silicon oxide films and nano-imprint textures, Phys. Status Solidi. 213 (2016) 1976–1982.

[22] A. Lambertz, V. Smirnov, T. Merdzhanova, K. Ding, S. Haas, G. Jost, R.E.I. Schropp, F. Finger, U. Rau, Microcrystalline silicon-oxygen alloys for application in silicon solar cells and modules, Sol. Energy Mater. Sol. Cells. 119 (2013) 134–143.

[23] K. Ding, U. Aeberhard, F. Finger, U. Rau, Silicon heterojunction solar cell with amorphous silicon oxide buffer and microcrystalline silicon oxide contact layers, Phys. Status Solidi - Rapid Res. Lett. 6 (2012) 193–195.

[24] P. Buehlmann, J. Bailat, D. Dominé, A. Billet, F. Meillaud, A. Feltrin, C. Ballif, In situ silicon oxide based intermediate reflector for thin-film silicon micromorph solar cells, Appl. Phys. Lett. 91 (2007) 143505.

[25] V. Smirnov, A. Lambertz, B. Grootoonk, R. Carius, F. Finger, Microcrystalline silicon oxide (μc-SiOx:H) alloys: A versatile material for application in thin film silicon single and tandem junction solar cells, J. Non. Cryst. Solids. 358 (2012) 1954–1957.

[26] Z.C. Holman, M. Filipič, A. Descoeudres, S. De Wolf, F. Smole, M. Topič, C. Ballif, Infrared light management in high-efficiency silicon heterojunction and rear-passivated solar cells, J. Appl. Phys. 113 (2013) 1–13.

[27] F.-J. Haug, T. Söderström, O. Cubero, V. Terrazzoni-Daudrix, C. Ballif, Plasmonic

absorption in textured silver back reflectors of thin film solar cells, J. Appl. Phys. 104 (2008) 64509.

[28] V. Smirnov, A. Lambertz, F. Finger, Electronic and Structural Properties of n-type Microcrystalline Silicon Oxide Films for Applications in Thin Film Silicon Solar Cells, in: Energy Procedia, 2015: pp. 71–77. doi:10.1016/j.egypro.2015.12.297.

[29] B. Gault, M.O. Moody, J.M. Cairney, S.P. Ringer, Atom Probe Microscopy, Springer, 2012.

[30] T. Kinno, M. Tomita, T. Ohkubo, S. Takeno, K. Hono, Laser-assisted atom probe tomography of 18O-enriched oxide thin film for quantitative analysis of oxygen, Appl. Surf. Sci. 290 (2014) 194–198.

[31] O. Gabriel, S. Kirner, M. Klingsporn, F. Friedrich, B. Stannowski, R. Schlatmann, On the Plasma Chemistry During Plasma Enhanced Chemical Vapor Deposition of Microcrystalline Silicon Oxides, Plasma Process. Polym. 12 (2015) 82–91.

[32] P. Delli Veneri, L.V. Mercaldo, I. Usatii, Silicon oxide based n-doped layer for improved performance of thin film silicon solar cells, Appl. Phys. Lett. 97 (2010) 23512.

[33] A. Richter, L. Zhao, F. Finger, K. Ding, Nano-composite microstructure model for the classification of hydrogenated nanocrystalline silicon oxide thin films, Surf. Coatings Technol. 295 (2015) 119–124.

[34] M.K. Miller, R.G. Forbes, Atom probe tomography, Mater. Charact. 60 (2009) 461–469.

[35] X.J. Hao, E.-C. Cho, C. Flynn, Y.S. Shen, G. Conibeer, M.A. Green, Effects of boron doping on the structural and optical properties of silicon nanocrystals in a silicon dioxide matrix., Nanotechnology. 19 (2008) 424019.

[36] R. Saleh, N.H. Nickel, The influence of boron concentrations on structural properties in disorder silicon films, Appl. Surf. Sci. 254 (2007) 580–585.

[37] B. Goldstein, C.R. Dickson, I.H. Campbell, P.M. Fauchet, Properties of p+ microcrystalline films of SiC:H deposited by conventional rf glow discharge, Appl. Phys. Lett. 53 (1988) 2672–2674.

[38] S.M. Iftiquar, The roles of deposition pressure and rf power in opto-electronic properties of a-SiO:H films, J. Phys. D. Appl. Phys. 31 (1998) 1630.

[39] A. Richter, M. Hermle, S.W. Glunz, Reassessment of the limiting efficiency for crystalline silicon solar cells, IEEE J. Photovoltaics. 3 (2013) 1184–1191.

[40] F. Urbain, K. Wilken, V. Smirnov, O. Astakhov, A. Lambertz, J.-P. Becker, U. Rau, J. Ziegler, B. Kaiser, W. Jaegermann, F. Finger, Development of Thin Film Amorphous Silicon Tandem Junction Based Photocathodes Providing High Open-Circuit Voltages for Hydrogen Production, Int. J. Photoenergy. 2014 (2014) 1–10.

Fig. 1. Schematic layer stacks for (a) a silicon heterojunction (SHJ) and (b) a Si thin-film (TF) triple-junction solar cell with indicated potential applications of nc-SiO_x:H layers. These are: I) front surface field (FSF) / front-emitter layer, II) back surface field (BSF) / rear-emitter layer, III) first interlayer, IV) intermediate reflector (IR), and V) back contact (BC) layer.

Fig. 2. Electrical and optical properties of several n- (circles) and p-type (squares) nc-SiO_x:H films deposited on glass. Stars indicate the films that were used as front surface field (FSF) layers, emitter layers, back contact (BC) layers, or intermediate reflectors (IR) in this study. The added lines serve as guides to the eye and roughly outline the performance limits of the films.

Fig. 3. Si density map of a 75x20x2 nm^3 slice from the APT tip of an n-type (a) and a p-type (b) nc-SiO_x:H film. Si iso density surfaces of 49.9 nm^{-3} (turqoise) were overlayed to approximate the nc-Si phase. Red arrows indicate the direction of film growth.

Fig. 4. Three-dimensional Si iso density surfaces (turqoise) of an n-type (a) and a p-type (b) nc-SiO_x:H film in cubes of 30x30x30 nm^3. The positions of P and B are indicated by red and orange circles, respectively. The red arrow indicates the direction of film growth. c) Proximity histogram of P and C with respect to the nc-Si surfaces for the n-type nc-SiO_x:H film. Negative distances represent locations within the nc-Si phase as defined by the Si iso density surfaces. d) Proximity histogram of B and C for the p-type nc-SiO_x:H film.

Fig. 5. External quantum efficiency and absorptance for a rear-emitter silicon heterojunction solar cell with a nc-SiO_x:H front surface field and a nc-SiO_x:H emitter layer. The inset lists the short circuit current density J_{sc} as determined via the *EQE* spectrum, the fill factor *FF*, the open circuit voltage V_{oc}, and the active area solar energy conversion efficiency η_{act} of the solar cell.

Fig. 6. External quantum efficiency (*EQE*) of the sub-cells and the total *EQE* for an a-Si:H/a-Si:H/µc-Si:H triple-junction solar cell with an n-type nc-SiO_x:H intermediate reflector (IR) and an n-type nc-SiO_x:H back contact (BC) layer. The inset lists the short circuit current density J_{sc} as determined via the *EQE* spectrum, the fill factor *FF*, the open circuit voltage V_{oc}, and the solar energy conversion efficiency η of the solar cell.

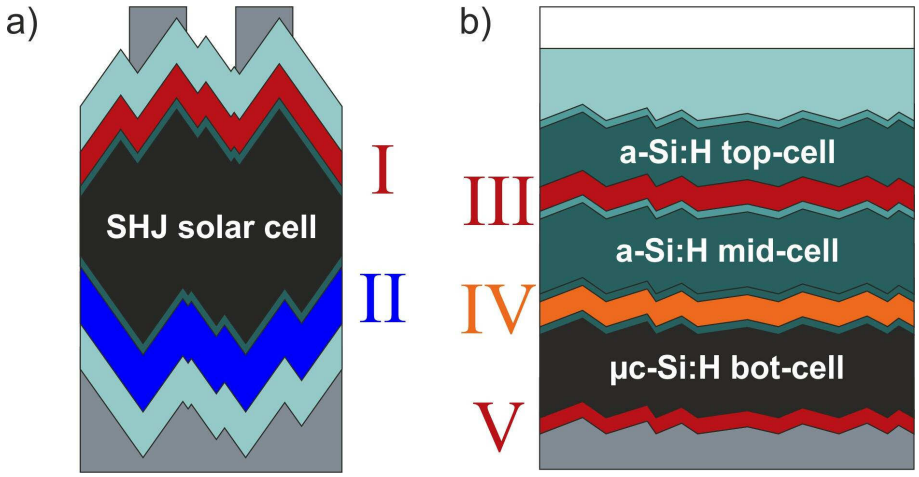
a)
SHJ solar cell
I
II
b)
III
IV
V
a-Si:H top-cell
a-Si:H mid-cell
µc-Si:H bot-cell

Fig. 1.

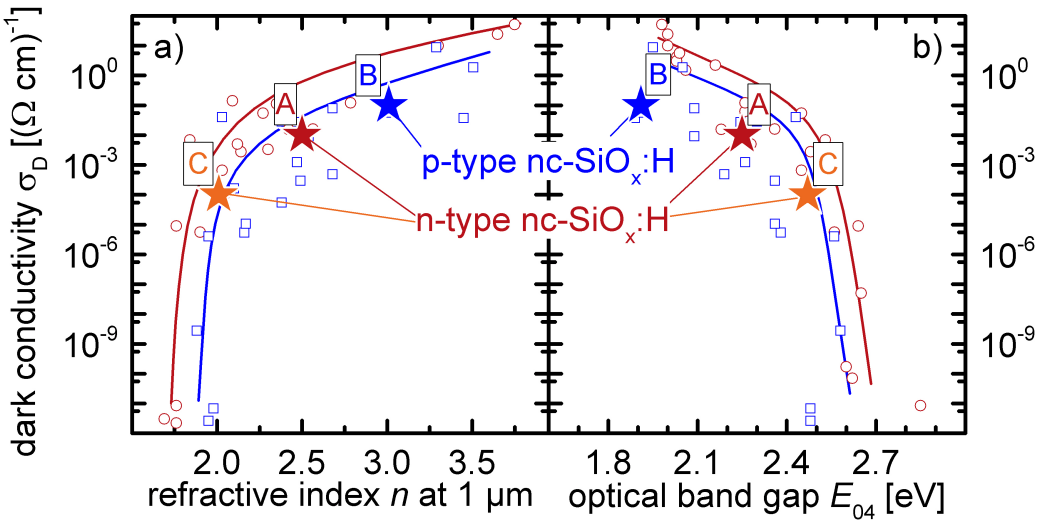
dark conductivity σ_D [(Ω cm)$^{-1}$]
a)
b)
A
B
C
p-type nc-SiO$_x$:H
n-type nc-SiO$_x$:H
refractive index n at 1 µm
optical band gap E_{04} [eV]

Fig. 2.

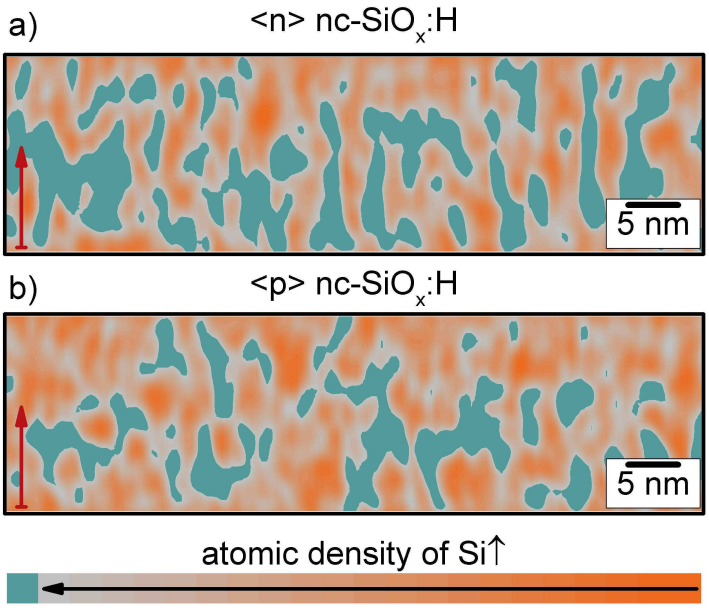
a)
<n> nc-SiO$_x$:H
5 nm
b)
<p> nc-SiO$_x$:H
5 nm
atomic density of Si↑

Fig. 3.

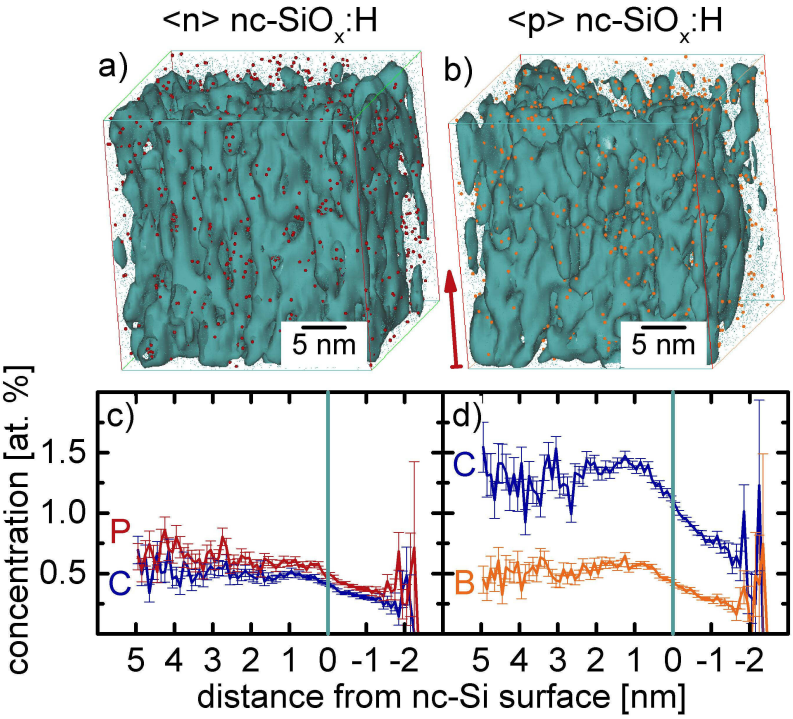
<n> nc-SiO$_x$:H
<p> nc-SiO$_x$:H
a)
b)
5 nm
5 nm
c)
d)
concentration [at. %]
1.5
1.0
0.5
P
C
C
B
5 4 3 2 1 0 -1 -2
5 4 3 2 1 0 -1 -2
distance from nc-Si surface [nm]

Fig. 4.

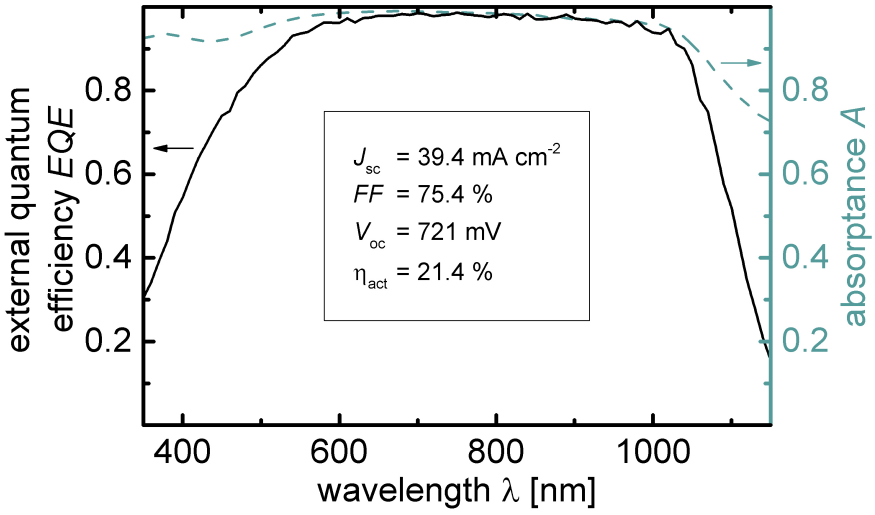
external quantum efficiency EQE
absorptance A
wavelength λ [nm]
J_{sc} = 39.4 mA cm^{-2}
FF = 75.4 %
V_{oc} = 721 mV
η_{act} = 21.4 %

Fig. 5.

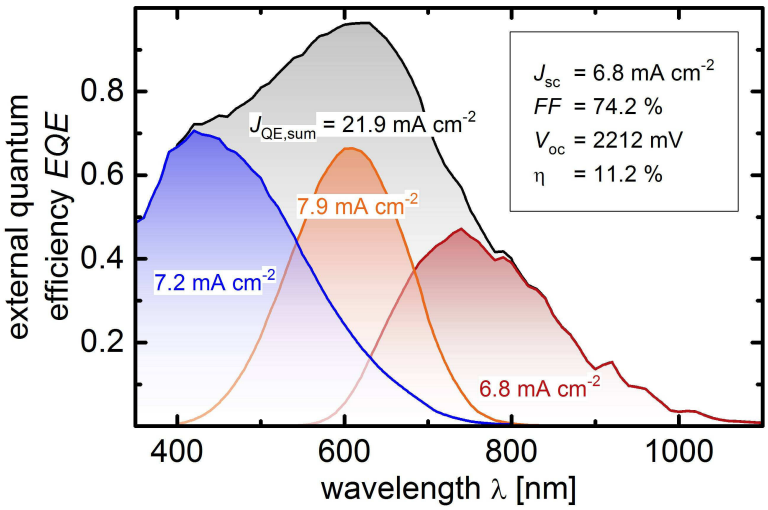
external quantum efficiency EQE
wavelength λ [nm]
$J_{QE,sum}$ = 21.9 mA cm^{-2}
7.2 mA cm^{-2}
7.9 mA cm^{-2}
6.8 mA cm^{-2}
J_{sc} = 6.8 mA cm^{-2}
FF = 74.2 %
V_{oc} = 2212 mV
η = 11.2 %

Fig. 6.